

Current-driven writing process in antiferromagnetic Mn_2Au for memory applications

S. Reimers^{†,1} Y. Lytvynenko^{†,1,2} Y. R. Niu,³ E. Goliás,³ B. Sarpi,⁴ L. S. I. Veiga,⁴
T. Denneulin,⁵ A. Kovács,⁵ R. E. Dunin-Borkowski,⁵ J. Bläßer,¹ M. Kläui,¹ and M. Jourdan^{*1}

¹*Institut für Physik, Johannes Gutenberg-Universität Mainz, 55099 Mainz, Germany*

²*Institute of Magnetism of the NAS of Ukraine and MES of Ukraine, 03142 Kyiv, Ukraine*

³*MAX IV Laboratory, Fotogatan 8, 22484 Lund, Sweden*

⁴*Diamond Light Source, Chilton, Didcot, Oxfordshire, OX11 0DE, United Kingdom*

⁵*Ernst Ruska-Centre for Microscopy and Spectroscopy with Electrons,
Forschungszentrum Jülich, 52425 Jülich, Germany*

Current pulse driven Néel vector rotation in metallic antiferromagnets is one of the most promising concepts in antiferromagnetic spintronics. We show microscopically that the Néel vector of epitaxial thin films of the prototypical compound Mn_2Au can be reoriented reversibly in the complete area of cross shaped device structures using single current pulses. The resulting domain pattern with aligned staggered magnetization is long term stable enabling memory applications. We achieve this switching with low heating of ≈ 20 K, which is promising regarding fast and efficient devices without the need for thermal activation. Current polarity dependent reversible domain wall motion demonstrates a Néel spin-orbit torque acting on the domain walls.

* email: Jourdan@uni-mainz.de

[†] These authors contributed equally to this work.

INTRODUCTION

Novel storage concepts in spintronics based on antiferromagnets (AFMs) propose to encode information by the direction of the alignment of the staggered magnetization or Néel vector [1–4]. This approach takes advantage of the intrinsically fast THz dynamics of AFMs [5] and their stability against external magnetic fields (see e. g. [6]). The interest in such concepts has grown strongly with the prediction of a so called Néel spin-orbit torque (NSOT) in metallic collinear AFMs with a specific symmetry, which is expected to rotate the spins of the AFM sublattices in a perpendicular orientation with respect to a driving bulk current [7].

Correspondingly, within the first generation of experiments on both known compounds with the required structure and AFM ordering, CuMnAs and Mn_2Au , current pulse induced reversible resistance modifications were reported as evidence for NSOT driven Néel vector rotation [8–13]. However, it later became clear that alternative mechanisms such as current pulse induced heat effects [14, 15], electromigration [16], and rapid quenching induced structural and magnetic modifications [17] can result in resistance modifications similar to the ones reported as well. Additionally, external strain supported Néel vector manipulation in Mn_2Au was demonstrated [18, 19]. Thus, microscopic investigations showing the intended current driven alignment of the staggered magnetization directly are essential. Up to now, for CuMnAs as well as for Mn_2Au , only minor current induced modifications were observed, i. e. only a small fraction of the antiferromagnetic domains switched with limited reversibility and stability [9, 20]. This is neither sufficient

regarding the identification of the switching mechanism as local inhomogeneities are involved nor does it demonstrate the applicability of current induced Néel vector switching for memory devices.

Furthermore, microscopic imaging provides direct insights into the current driven mechanisms of Néel vector reorientation [21]. This recently attracted renewed interest, as in NiO/Pt bilayers thermomagnetoelastic coupling effects were observed, which act in a very similar way as spin-orbit torques on the Néel vector [22]. Thus, the experimental demonstration of a current induced NSOT is important.

Here we show current pulse induced complete, remanent, and reversible Néel vector switching of $\text{Mn}_2\text{Au}(001)$ thin films patterned in cross-structures, which is compatible with spintronics applications such as magnetic random access memory (MRAM). A current polarity dependence demonstrates an NSOT acting on AFM domain walls. Studying different pulse lengths, we show that in contrast to related experiments on Mn_2Au [12], for our epitaxial thin films thermal activation is not necessary for switching, which is important for fast and energy efficient memory applications regarding potential ultrafast applications.

RESULTS

Mn_2Au is a metallic antiferromagnet with a high Néel temperature above 1000 K [23]. The compound has a tetragonal crystal structure with two equivalent $\langle 110 \rangle$ easy axes in the (001)-plane and a strong out-of-plane magnetic anisotropy.

We investigate epitaxial $\text{Mn}_2\text{Au}(001)$ thin films with a thickness of 45 nm grown on an epitaxial double buffer layer of 13 nm of $\text{Ta}(001)$ on 20 nm of $\text{Mo}(001)$ on $\text{MgO}(001)$ substrates (see Supplementary Information).

The samples are capped with 2 nm of SiN_x and patterned by optical lithography and Argon ion beam etching.

The largest NSOT is expected for the current directions parallel and antiparallel to the Néel vector [7, 24]. Correspondingly, we patterned a $\text{Mn}_2\text{Au}(001)$ thin film in a cross structure oriented parallel to the easy $\langle 110 \rangle$ directions, which allows to send current pulses both parallel and perpendicular to the axis along which the Néel vector is aligned. We obtain a repeatable complete switching of the Néel vector orientation in the central area ($10\ \mu\text{m} \times 10\ \mu\text{m}$) of the cross by applying current pulses alternating between the two orthogonal directions. Fig. 1 shows X-ray magnetic linear dichroism - photoelectron emission microscopy (XMLD-PEEM) images obtained after subsequent pulses, in which the 90° reorientation of the Néel vector shows up as alternating dark and white contrast of the central area.

For the investigation of the role of current heating induced thermal activation [12], we compare current pulse trains with different numbers and lengths, ranging from a train of 100 pulses with a lengths of 1 ms down to a single $10\ \mu\text{s}$ pulse. The panels **a** and **b** of Fig. 1 show an example of complete switching after a train of 100 current pulses with a length of 1 ms each (off time after each pulse 10 ms). The panels **c** and **d** show very similar switching obtained after a single bipolar current pulse with a length of $10\ \mu\text{s}$ only. Although only a single pulse instead of 100 pulses was used and the pulse length was 100 times shorter, the required current densities to obtain complete Néel vector rotation are very similar with $J_{1\text{ms}} \approx 2.6 \times 10^{11}\ \text{A/m}^2$ and $J_{10\ \mu\text{s}} \approx 3.0 \times 10^{11}\ \text{A/m}^2$ (and $J_{100\ \mu\text{s}} \approx 2.7 \times 10^{11}\ \text{A/m}^2$, not shown). These current densities and pulse lengths result in significantly different temperature increases of the Mn_2Au thin film due to ohmic heating with $\Delta T(1\ \text{ms}) \approx 70\ \text{K}$, $\Delta T(100\ \mu\text{s}) \approx 45\ \text{K}$, and $\Delta T(10\ \mu\text{s}) \approx 20\ \text{K}$, as determined from ex-situ reference resistance measurements during application of current pulses (see Supplementary Information).

Next we investigate how the switched area of the sample depends on the current density. We patterned a single stripe along an easy $[110]$ direction of a Mn_2Au thin film and applied 1 ms current pulses with increasing current density, as shown in Fig. 2. The single stripe geometry ensures a homogeneous distribution of the current density. The transition from the beginning of Néel vector reorientation to complete switching with increasing pulse current density occurs within a range of $\approx 20\%$ of the maximum required current.

The left panel of Fig. 2 shows the initial domain configuration, in the as grown state after patterning. It is characterised by a preferential alignment of the Néel vector parallel to the stripe, which originates from patterning induced anisotropy [26]. With increasing amplitude of the current pulses (panels from left to right in Fig. 2), the first reorientation of the Néel vector appears in some central regions of the stripe indicated by yellow circles

with a current density of $J_{1\text{ms}} = 2.46 \times 10^{11}\ \text{A/m}^2$. With further increasing current, the switched area increases homogeneously distributed over the patterned area, consistent with the absence of patterning induced current inhomogeneities. In the same experiment with an MBE grown $\text{Mn}_2\text{Au}(001)$ thin film [28] and shorter current pulses ($20\ \mu\text{s}$) very similar results were obtained, showing the robustness of the switching properties.

In order to identify if the switching is driven by NSOT, we investigated the current direction and polarity dependence of the Néel vector reorientation. This allows us to compare the experimental results of changes to the AFM domains and domain wall positions to theoretical predictions for NSOT [7, 24]. Current pulses were applied along a hard $[100]$ direction of a $\text{Mn}_2\text{Au}(001)$ thin film using a single patterned stripe aligned along this direction. In this geometry, no net alignment of the Néel vector was obtained in the central region of the patterned stripe. However, we observed a partial current polarity dependent reversible reorientation. Some of these regions which switch for positive current polarity from vertical to horizontal alignment are indicated by the red circles in Fig. 3. Examples of other regions which switch in the opposite direction are indicated by yellow circles. The green circles in panel **f** show regions, in which the current was flowing preferentially along an easy $\langle 110 \rangle$ -direction resulting in a local alignment of the Néel vector corresponding to the behavior discussed above (Figs. 1 and 2).

Finally, we determine the change of the sample resistance associated with the Néel vector reorientation discussed above. For this, an 8-terminal shaped device as shown in panel **b** of Fig. 4 was patterned. We applied bipolar current pulses alternating between the two orthogonal easy $\langle 110 \rangle$ directions, as done previously for the 4-terminal cross structures shown in Fig. 1. With the 8-terminal geometry, both the longitudinal R_{long} as well as the transversal R_{trans} sample resistance can be probed after each current pulse as shown in Fig. 4. Pulsing with the same current densities as required for the observation of the Néel vector reorientation by X-PEEM, we observed alternating longitudinal (panel **a**) as well as transversal (see Supplementary Material) resistance values. Both magnetoresistance signals are as expected of similar magnitude, slightly inhomogeneous Néel vector alignment in the central area of the 8-terminal cross might explain the remaining differences. We obtained a maximum $\Delta R_{\text{long}}/R_{\text{long}} \simeq 1 \times 10^{-3}$, which is consistent with the low temperature anisotropic magnetoresistance value of $\text{AMR}_{\text{Mn}_2\text{Au}} \simeq -1.5 \times 10^{-3}$, which we obtained previously by aligning the Néel vector with a 50 T magnetic field pulse [27]. Furthermore, the negative AMR of Mn_2Au (i. e. $\rho_{\perp} > \rho_{\parallel}$) is consistent with the larger longitudinal resistance in Fig. 4 (panel **a**) associated with pulse current direction I_{pulse1} (blue data points), if the Néel vector is aligned perpendicular to the current direc-

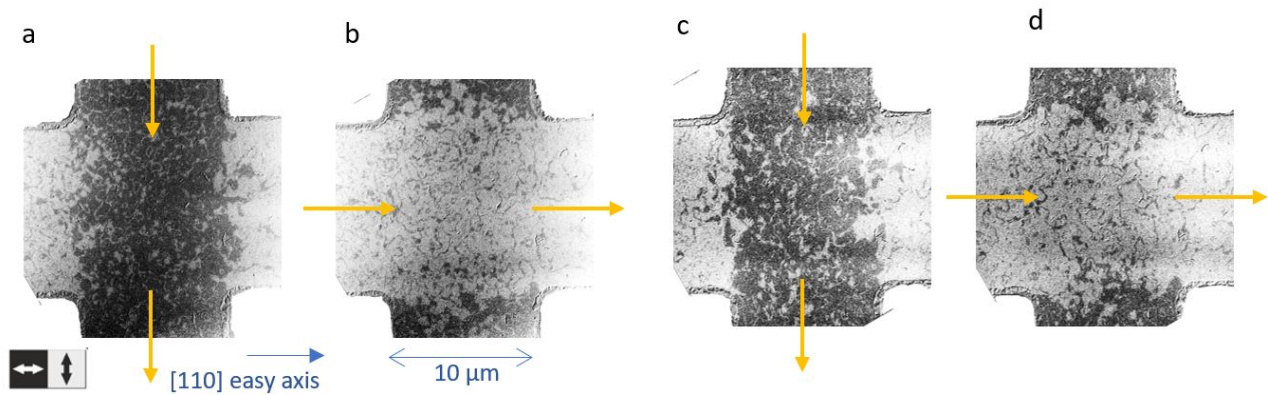


FIG. 1. XMLD-PEEM images of reversible Néel vector reorientation, with current parallel easy axes. The images show the orientation of the Néel vector of $\text{Mn}_2\text{Au}(001)$ thin films after sending current pulses with different length and direction (yellow arrows) through a patterned cross structure oriented parallel to the easy $\langle 110 \rangle$ directions. The dark regions correspond to a horizontal, the bright regions to a vertical alignment of the Néel vector as indicated below panel **a** by the double arrows. **a, b**: After 100 pulses of 1 ms length each with a current density of $J = 2.6 \times 10^{11} \text{ A/m}^2$. **c, d**: After 1 bipolar pulse of $10 \mu\text{s}$ length with a current density of $J = 3.0 \times 10^{11} \text{ A/m}^2$.

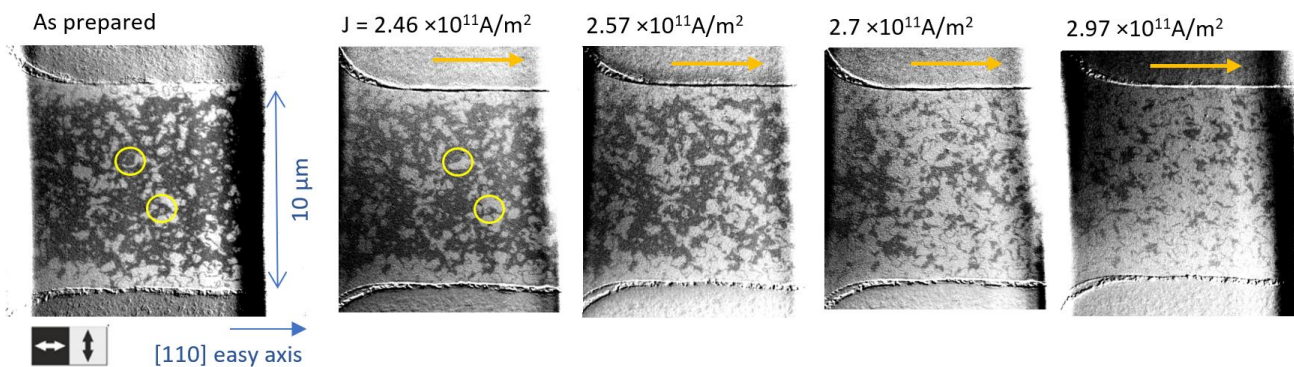


FIG. 2. XMLD-PEEM images of Néel vector reorientation, with current along easy axis. The images show the orientation of the Néel vector of $\text{Mn}_2\text{Au}(001)$ thin films as grown and after sending current pulses (length 1 ms) with increasing amplitude along an easy $\langle 110 \rangle$ direction through a patterned stripe structure. The yellow arrows indicate the current directions.

tion as expected for an NSOT acting.

Furthermore, consistent with the X-PEEM measurements, the electrical signal shows no sign of decay as shown in the Supplementary Information.

DISCUSSION

For potential spintronics applications such as antiferromagnetic random access memory (MRAM), long term stability of the Néel vector aligned states is required. In this framework our $\text{Mn}_2\text{Au}(001)$ thin films are very suitable as the current pulse induced AFM domain configurations perfectly fulfill this requirement. We were able to demonstrate by XMLD-PEEM that even four months after the current pulse Néel vector alignment shown in Fig. 2, the aligned AFM domain configuration was preserved (see Supplementary Information). Furthermore, already single current pulses are able to reorient the Néel

within the central area of device cross shaped structures completely and reversibly, i. e. again fulfilling the requirements for applications.

For spintronics, the size of the electrical read-out signal associated with Néel vector reorientation is of major importance. Our work confirms that the maximum obtainable signal from AMR is relatively small so that in antiferromagnetic spintronics other read-out mechanisms, for example via an adjacent strongly exchange-coupled ferromagnetic layer as discussed in reference [29], need to be considered. Furthermore, our small electrical read-out signals are clearly distinguishable from the current pulse induced large resistance modifications previously obtained investigating various non-NSOT related metals as mentioned in the introduction.

Regarding the physical mechanism of the current pulse induced Néel vector reorientation, we compare our experiments with theoretical predictions assuming an NSOT, which is expected to be largest for current direction par-

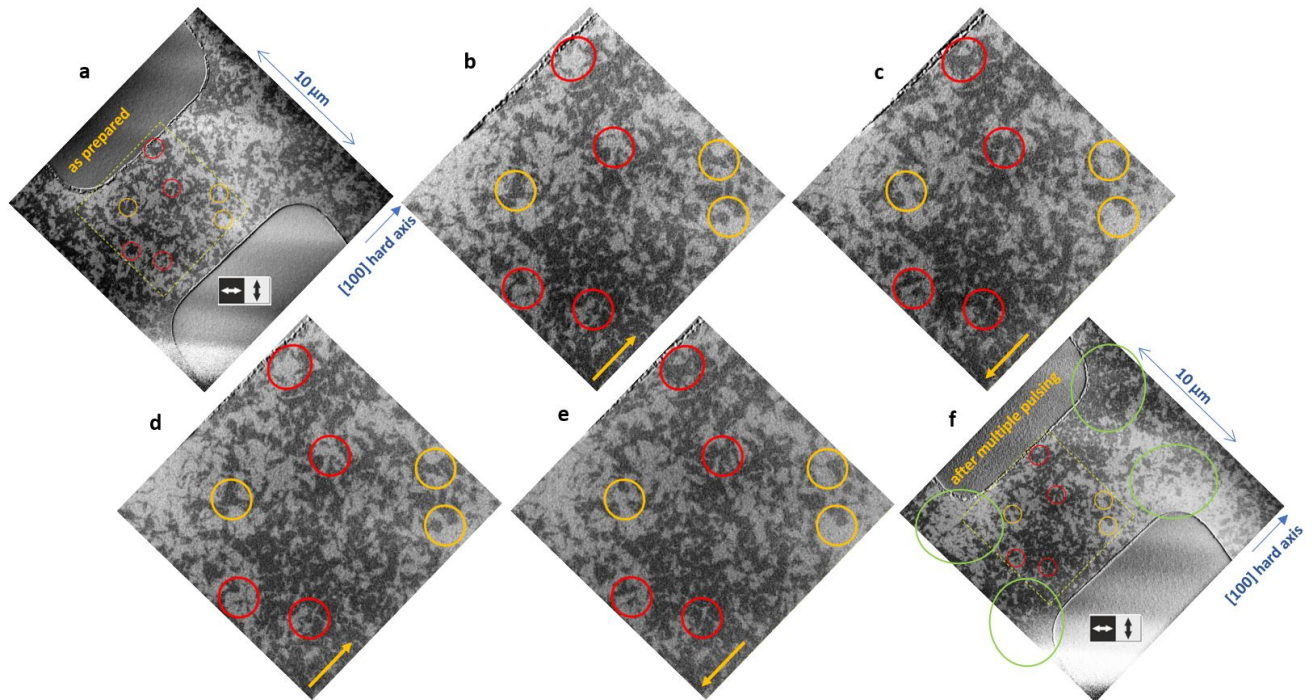


FIG. 3. XMLD-PEEM images of Néel vector reorientation, with current parallel hard axis. The images show the orientation of the Néel vector of $\text{Mn}_2\text{Au}(001)$ thin films as grown (panel a) and after sending current pulses (length 1 ms, amplitude $J = 3.6 \times 10^{11} \text{ A/m}^2$) with alternating polarity indicated by yellow arrows along the hard [100] direction through a patterned stripe structure with panels b to e showing the region indicated by the yellow dashed square in panel a with increased magnification. Panel f shows the full field of view after the last current pulse.

allel to the sublattice magnetization and zero for current perpendicular to it [7, 24]. Fully consistent with this prediction, we observe a current induced Néel vector orientation perpendicular to the pulse direction, if the current flows parallel to an easy $\langle 110 \rangle$ -axis of Mn_2Au (Figs. 1 and 2). However, also thermomagnetoelastic coupling effects driven by anisotropic strain due to current heating can generate this type of Néel vector reorientation [22], as the Néel vector prefers alignment along an elongated $\langle 110 \rangle$ direction [19]. In principle, thermomagnetoelastic coupling and NSOT can cooperate for stripe and cross geometries aligned along $\langle 110 \rangle$ directions.

To study the action of the NSOT independently from this potentially additional contribution, we discuss the reversible current polarity dependence of the Néel vector reorientation, which cannot appear due to any thermally driven effect which acts identically for both current directions. For current pulses parallel to a hard $\langle 100 \rangle$ -direction, the strongest NSOT is expected to act on the AFM domain walls, as only there the Néel vector is aligned parallel to the current. In this case the NSOT is expected to shift the domain wall reversibly with inverted current direction as observed previously for $\text{CuMnAs}(001)$ thin films [21]. As discussed above and shown in Fig. 3, we demonstrated such a current polarity dependent reorientation of the Néel vector as well. In Mn_2Au , a

relatively large number of domains shows reversible modifications, but also in our compound the domain walls are shifted by distances of only $\approx 1 \mu\text{m}$. This indicates that mechanisms such as domain wall pinning are competing with the NSOT acting on the domain walls. Nevertheless, the reversible current polarity dependent Néel vector reorientation represents direct evidence for the action of a current induced NSOT.

In contrast to domain wall pinning, the potential barrier for Néel vector reorientation which is typically considered in theoretical work [7, 25] is the in-plane magnetocrystalline anisotropy ($\approx 1.8 \mu\text{eV}$ per formula unit for $\text{Mn}_2\text{Au}(001)$ [29]). In this framework a key role of thermal activation was previously reported based on investigations of granular Mn_2Au thin films [12]. However, as shown e.g. by the transmission electron microscopy image in the Supplementary Information, our $\text{Mn}_2\text{Au}(001)$ thin films are highly epitaxial without morphological feature on the typical length scale of the AFM domains, so that independent switching of morphological grains can be excluded. This strongly suggests that the reorientation occurs via domain wall motion.

Independent of the physical origin of the potential barriers to be overcome, it is important for spintronics applications that the current induced Néel vector reorientation does not depend on slow thermal activation processes.

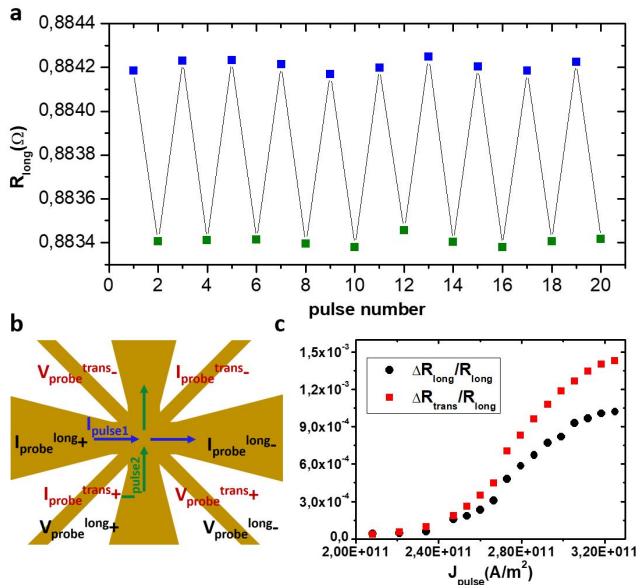


FIG. 4. **Switching induced anisotropic magnetoresistance.** Panel **a** shows the alternating longitudinal resistance of a Mn_2Au thin film patterned in the geometry shown in panel **b**. The longitudinal resistance was measured after each 1 ms current pulse with $J_{\text{pulse}} = 3 \times 10^{11}$ A/m² applied alternately in perpendicular directions as indicated by the blue and green arrows in panel **b**. The color of the data points corresponds to the arrows indicating the current direction. Panel **c** shows the dependence of the longitudinal ΔR_{long} as well as of the transverse ΔR_{trans} resistance changes on the pulse current density J_{pulse} .

Here, the required current density for full Néel vector reorientation using a single 10 μs current pulse was only $\approx 10\%$ larger than required for a pulse train of 100 current pulses with 1 ms pulse length each. This indicates that the current pulse induced force is at least of the same order of magnitude as opposing forces e.g. due to domain wall pinning.

We have shown that metallic antiferromagnets, specifically epitaxial $\text{Mn}_2\text{Au}(001)$ thin films, are finally able to fulfill one of the major early promises of antiferromagnetic spintronics: it is possible to write long term stable information by single current pulses into macroscopic areas of device structures. Regarding the switching mechanism, while thermomagnetoelastic contributions might be present, we identify a Néel spin-orbit torque acting on the domain walls leading to reversible motion. Furthermore, we have shown that thermal activation processes are not essential for current induced Néel vector reorientation, thereby enabling fast and energy efficient switching. Thus, epitaxial $\text{Mn}_2\text{Au}(001)$ thin films fulfill all requirements for memory applications regarding the writing and storage of data using a single antiferromagnetic layer.

METHODS

All experimental data shown in this manuscript was obtained investigating $\text{Mn}_2\text{Au}(001)(45\text{ nm})$ thin films grown epitaxially on $\text{Ta}(001)(13\text{ nm})/\text{Mo}(001)(20\text{ nm})$ double buffer layers on $\text{MgO}(100)$ substrates. All layers were deposited by magnetron sputtering by the process described in detail in ref. [29]. The samples were capped with 2 nm of polycrystalline SiN_x to protect them from oxidation. Optical lithography and ion beam etching were used to pattern the films into the cross and stripe structures shown in this manuscript.

Antiferromagnetic domain imaging was performed by combining photoemission electron microscopy with x-ray magnetic linear dichroism (XMLD-PEEM) at the Mn $L_{2,3}$ absorption edge at the PEEM endstations at beamline MAXPEEM at MAX IV, and beamline I06 at Diamond Light Source. The XMLD effect at the Mn $L_{2,3}$ absorption edge in Mn_2Au was established in previous work. For x-ray polarisation along a Mn_2Au $\langle 110 \rangle$ direction, the Mn $L_{2,3}$ XMLD spectrum shows a minimum and a maximum located at the absorption edge E_{max} and at 0.8 eV below the edge. At MAXPEEM, the x-ray beam has normal incidence at the sample surface. The XMLD-PEEM images obtained at this beamline are the asymmetry images of images taken with two orthogonal x-ray polarisations along the $\langle 110 \rangle$ directions and energy of $h\nu = E_{\text{max}} - 0.8\text{ eV}$, as this provides maximum contrast and minimum sensitivity to morphological features. At I06, the x-ray beam is incident at a grazing angle of 16° . XMLD-PEEM images measured there are the asymmetry of images with photon energies of $h\nu = E_{\text{max}}$ and $h\nu = E_{\text{max}} - 0.8\text{ eV}$ for fixed in-plane polarisation along a $\langle 110 \rangle$ direction.

In-situ electrical manipulation was performed using the pulse functions of Keithley2601B-PULSE (at MAX IV) and Keithley 2461 (at Diamond) sourcemeters, integrated into the X-PEEM setup.

The ex-situ resistance measurements (Fig. 4) were performed using a Keithley 6220 precision current source with a probe current of 50 μA and a Keithley 2182A Nanovoltmeter in Delta mode averaging over 200 measurements to obtain one data point. For automatising the pulse (Keithley 2430 Pulse Source Meter) - probe sequence an Agilent 34970A Switch Unit was used.

For the quantification of the current pulse induced sample heating, we used a lithographic pattern, which additional to the cross shown in Fig. 1 contains four thin leads enabling longitudinal resistance measurements of the central cross area with a 4-probe technique (see Fig. 1 of ref. [11]). The maximum resistance obtained at the end of the current pulses with different lengths and amplitudes is shown in the Supplementary Information. By comparing this high pulse current sample resistance with the above room temperature linear extrapolated temper-

ature dependent sample resistance $R(T)$ obtained from a low current measurement in a cryostat, we can deduce the current pulse induced temperature raise. These measurements were performed outside the PEEM at ambient conditions using the same Keithley 2601B-PULSE Source Meter as for pulsing in the PEEM. The time dependent sample resistance during the current pulses was measured with an oscilloscope and using the SENSE inputs of the Source Meter obtaining consistent results.

SUPPLEMENTARY INFORMATION

Current pulse induced sample heating

All current pulsing experiments are associated with ohmic heating of the sample. As Mn_2Au is a metal with an almost linear resistance versus temperature relation, the current pulse induced heating can be measured via a resistance measurement during the pulse as described in the Methods section. Fig. S1 shows the relative resistance increase of a $\text{Mn}_2\text{Au}(001)$ sample patterned in a cross structure with a central section of $10\ \mu\text{m} \times 10\ \mu\text{m}$ as in Fig. 1 of the main text, but with additional leads to enable 4-probe resistance measurements. Different pulse lengths and amplitudes result in different heating. The dashed vertical lines in the main figure indicate the required current densities for complete switching of the Néel vector. From comparison with the extrapolated temperature dependent resistance measurement shown in the inset, the indicated temperatures associated with the switching using different pulse lengths are shown in the main panel.

Probing Néel vector reorientation by transverse resistance measurements

Electrical detection of current pulse induced Néel vector alignment is also possible via measurements of the transverse resistance or planar Hall-Effect. Considering the rather small electrical signal, this is more easy to measure than the longitudinal AMR, as there is no offset voltage. In Fig. S2, the measurement of the transverse resistance changes is shown in analogy to Fig. 4 of the main text.

Stability of the Néel vector alignment

All images of current induced Néel vector reorientation shown in the main text were obtained at MAX-PEEM (MAX IV). Four months later at Diamond Light Source, we were able to image the sample shown in Fig. 2 of the main text again. As shown in Fig. S3, we observed exactly the same domain pattern again, i. e. the current induced Néel vector oriented domain configuration obtained four month ago was completely preserved.

Additionally, we demonstrate the absence of relaxation on short time scales, i. e. seconds, by measurements of the transverse resistance after a sequence of current pulse induced reversible switching. The data shown in Fig. S4 was obtained in the same way as for Fig. S2 (here with

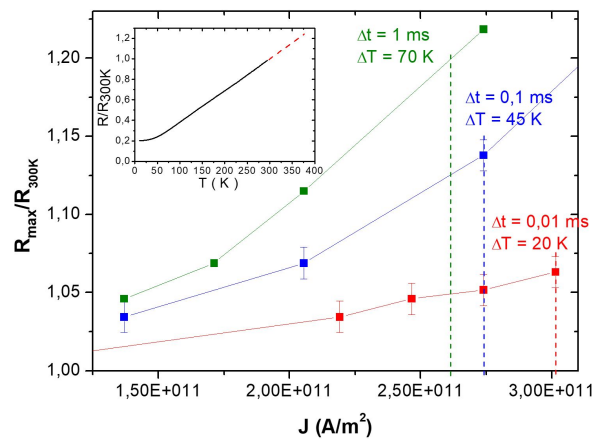


FIG. 5. **S1: Current pulse induced sample heating.** The measurements in the main panel show the maximum sample resistance (normalized to the 300 K resistance) during application of current pulses with different length and amplitude. The dashed vertical lines show the required currents for full Néel vector reorientation corresponding to Fig. 1. The inset shows the temperature dependence of the normalized resistance obtained from a standard dc measurement. Its extrapolation (red dashed line) is used to convert the resistance increase during current pulsing into a temperature increase ΔT shown in the graph.

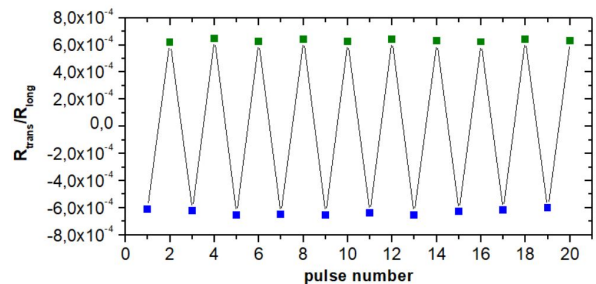


FIG. 6. **S2: Switching induced planar Hall effect.** The measurements show the alternating transverse resistance of a Mn_2Au thin film patterned in the geometry shown in Fig. 4, panel b. The transverse resistance was measured after each 1 ms current pulse with $J_{\text{pulse}} = 3 \times 10^{11}\ \text{A/m}^2$ applied alternately in perpendicular directions as indicated by the blue and green arrows in Fig. 4, panel b. The color of the data points corresponds to the arrows indicating the current direction.

$J_{\text{pulse}} = 2.9 \times 10^{11}\ \text{A/m}^2$), but we kept measuring the resistance after the last switching current pulse for 1.5 h. The raw data shown was obtained at a sampling rate of ≈ 2 data points per second. Also on this time scale, no relaxation of the resistance after the last switching pulse was observed.

Microstructure of $\text{Mn}_2\text{Au}(001)$ thin films

All epitaxial Mn_2Au thin films used for this manuscript were prepared by sputtering as described in the Methods sections. Beyond their characterization shown in ref. [20], we here want to emphasize their long range crystallo-

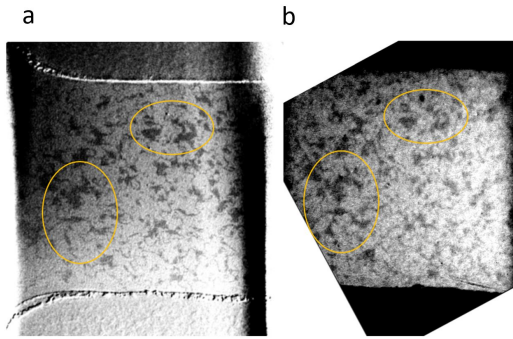


FIG. 7. **S3: Long term stability of switched state.** The XMLD-PEEM image in panel **a** is the same as shown in Fig. 2, right panel, obtained after current induces Néel vector reorientation. The image in panel **b** shows the same area 4 months later. The yellow circles serve to guide the eye showing exactly the same AFM domain pattern (please note that the image in panel **b** has reduced magnetic contrast due to a different PEEM geometry).

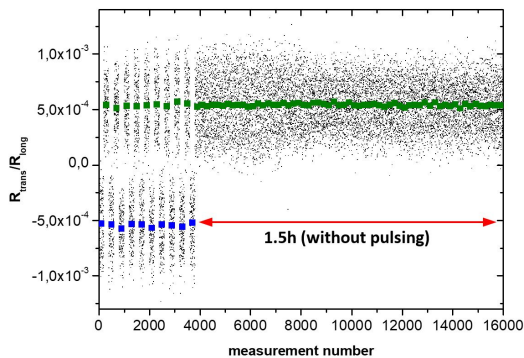


FIG. 8. **S4: Second time-scale stability of switched state.** Raw data (black data points) and averaged data points (over 200 raw data points) of the transverse resistance of a Mn_2Au thin film. Here, the transverse resistance was measured after each 1 ms current pulse with $J_{\text{pulse}} = 2.9 \times 10^{11}$ A/m² applied alternately in perpendicular directions followed by pure resistance measurements without pulsing. No relaxation was observed.

graphic order by showing in Fig. S5 scanning transmission electron microscopy images. Panel **a** with the highest magnifications shows the Mn_2Au lattice with atomic resolution (on top of this sample is a Permalloy layer, which was not present in the other samples discussed here.). Panel **b** with a larger field of view shows a MnAu impurity phase at the interface with the Ta buffer layer, which, however, does not disturb the growth of the Mn_2Au layer on top of it. Panel **c** shows the largest field of view demonstrating the long range coherence of the epitaxial growth.

For obtaining the STEM images, an electron transparent cross-section lamella was prepared using a 30 kV focused Ga⁺ ion beam and scanning electron microscope (FIB-SEM) FEI Helios platform. The ion beam energy

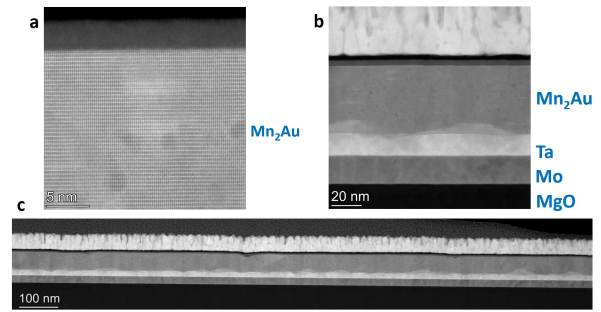


FIG. 9. **S5: Microstructure of a $\text{Mn}_2\text{Au}(001)$ epitaxial thin film.** Cross section HAADF STEM images with different magnifications showing the microstructure of an epitaxial $\text{Mn}_2\text{Au}(001)$ thin film. A weak MnAu impurity phase is visible at the interface between the Mn_2Au and the Ta buffer layer. The samples show long range crystallographic order.

was decreased to 5 kV for the final thinning steps. Scanning transmission electron microscopy (STEM) was carried out using an FEI Titan TEM equipped with a Schottky field emission gun operated at 200 kV, a CEOS probe aberration corrector and a high angle annular dark-field detector (HAADF).

Data availability

The raw data of the transport measurements shown in this study has been deposited in the Zenodo database under accession code DOI 10.5281/zenodo.7467238.

Acknowledgements

We acknowledge funding by the Deutsche Forschungsgemeinschaft (DFG, German Research Foundation) - TRR 173 - 268565370 (project A05, with contribution from A01), by the Horizon 2020 Framework Program of the European Commission under FET-Open Grant No. 863155 (s-Nebula), by EU HORIZON-CL4-2021-DIGITAL-EMERGING-01-14 programme under grant agreement No. 101070287, and by the TopDyn Center. We acknowledge MAX IV Laboratory for time on beamline MAXPEEM under Proposal 20210863, Diamond Light Source for time on beamline I06 under proposal MM30141-1, and Swiss Light Source for time on beamline SIM. Research conducted at MAX IV, a Swedish national user facility, is supported by the Swedish Research council under contract 2018-07152, the Swedish Governmental Agency for Innovation Systems under contract 2018-04969, and Formas under contract 2019-02496. The STEM investigations were funded by the European Union's Horizon 2020 Research and Innovation Programme under grant agreement 856538 (project "3D MAGIC").

Author contributions

S.R., Y.L., and M.J. wrote the paper, prepared the samples and performed the XMLD-PEEM investigations. Y.R.N and E.G. supported the XMLD-PEEM investigations at MAX IV, B.S. and L.S.I.V. at Diamond, and A.K. at SLS. S.R. and J.B. measured the Néel vector

induced resistance changes, Y.R.N. measured the pulse heating induced resistance changes. T.D., A.K. and R.E.D-B contributed the STEM investigations. M.K. contributed to the discussion of the results and provided input, M.J. coordinated the project.

Competing interests:

The authors declare no competing financial interests.

-
- [1] MacDonald, A. H., and Tsoi, M. Antiferromagnetic Metal Spintronics. *Philos. Trans. R. Soc. A* **369**, 3098 (2011).
- [2] Jungwirth, T., Sinova, J., Manchon, A., Marti, X., Wunderlich, J. and Felser, C. The multiple directions of antiferromagnetic spintronics, *Nat. Phys.* **14**, 200 (2018).
- [3] Baltz, V., Manchon, A., Tsoi, M., Moriyama, T., Ono, T., and Tserkovnyak, Y. Antiferromagnetic Spintronics. *Rev. Mod. Phys.* **90**, 015005 (2018).
- [4] Jungfleisch, M. B., Zhang, W., and Hoffmann, A. Perspectives of antiferromagnetic spintronics, *Phys. Lett. A* **382**, 865 (2018).
- [5] Kampfrath, T., Sell, A., Klatt, G., Pashkin, A., Mährlein, S., Dekorsy, T., Wolf, M., Fiebig, M., Leitenstorfer, A., and Huber, R. Coherent terahertz control of antiferromagnetic spin waves, *Nat. Phot.* **5**, 31 (2011).
- [6] Sapozhnik, A. A., Filianina, M., Bodnar, S. Yu., Lamirand, A., Mawass, M.-A., Skourski, Y., Elmers, H.-J., Zabel, H., Kläui, M., and Jourdan, M. Direct imaging of antiferromagnetic domains in Mn₂Au manipulated by high magnetic fields. *Phys. Rev. B* **97**, 134429 (2018).
- [7] Železný, J., Gao, H., Výborný, K., Zemen, J., Mäsek, J., Manchon, A., Wunderlich, J., Sinova, J., and Jungwirth, T. Relativistic Néel-Order Fields Induced by Electrical Current in Antiferromagnets, *Phys. Rev. Lett.* **113**, 157201 (2014).
- [8] Wadley, P., Howells, B., Železný, J., Andrews, C., Hills, V., Campion, R. P., Novák, V., Olejník, K., Maccherozzi, F., Dhesi, S. S., Martin, S. Y., Wagner, T., Wunderlich, J., Freimuth, F., Mokrousov, Y., Kuneš, J., Chauhan, J. S., Grzybowski, M. J., Rushforth, A. W., Edmonds, K. W., Gallagher, B. L., and Jungwirth, T. Electrical switching of an antiferromagnet. *Science* **351**, 587 (2016).
- [9] Grzybowski, M., Wadley, P., Edmonds, K. W., Beardley, R., Hills, V., Campion, R. P., Gallagher, B. L., Chauhan, J. S., Novák, V., and Jungwirth, T. Imaging Current-Induced Switching of Antiferromagnetic Domains in CuMnAs. *Phys. Rev. Lett.* **118**, 057701 (2017).
- [10] Matalla-Wagner, T., Rath, M.-F., Graulich, D., Schmalhorst, J.-M., Reiss, G. and Meinert, M. Electrical Néel-Order Switching in Magnetron-Sputtered CuMnAs Thin Films. *Phys. Rev. Appl.* **12**, 064003 (2019).
- [11] Bodnar, S. Yu., Šmejkal, L., Turek, I., Jungwirth, T., Gomonay, O., Sinova, J., Sapozhnik, A. A., Elmers, H.-J., Kläui, M., and Jourdan, M. Writing and reading antiferromagnetic Mn₂Au by Néel spin-orbit torques and large anisotropic magnetoresistance. *Nat. Commun.* **9**, 348 (2018).
- [12] Meinert, M., Graulich, D., and Matalla-Wagner, T. Electrical Switching of Antiferromagnetic Mn₂Au and the Role of Thermal Activation. *Phys. Rev. Appl.* **9**, 064040 (2018).
- [13] Zhou, X. F., Zhang, J., Li, F., Chen, X. Z., Shi, G. Y., Tan, Y. Z., Gu, Y. D., Saleem, M. S., Wu, H. Q., Pan, F., and Song, C. Strong Orientation-Dependent Spin-Orbit Torque in Thin Films of the Antiferromagnet Mn₂Au. *Phys. Rev. Appl.* **9**, 054028 (2018).
- [14] Chiang, C. C., Huang, S. Y., Qu, D., Wu, P. H. and Chien, C. L. Absence of Evidence of Electrical Switching of the Antiferromagnetic Néel Vector. *Phys. Rev. Lett.* **123**, 227203 (2019).
- [15] Zink, B. The Heat in Antiferromagnetic Switching. *Physics* **12**, 134 (2019).
- [16] Matalla-Wagner T., Schmalhorst, J.-M., Reiss, G., Tamura, N., Meinert, M. Resistive contribution in electrical-switching experiments with antiferromagnets. *Phys. Rev. Res.* **2**, 033077 (2020).
- [17] Kašpar, Z., Surýnek, M., Zubáč, J., Krizek, F., Novák, V., Campion, R. P., Wörnlé, M. S., Gambardella, P., Marti, X., Němec, P., Edmonds, K. W., Reimers, S., Amin, O. J., Maccherozzi, F., Dhesi, S. S., Wadley, P., Wunderlich, J., Olejník, K., and Jungwirth, T. Quenching of an antiferromagnet into high resistivity states using electrical or ultrashort optical pulses. *Nat. Elect.* **4**, 30, (2021).
- [18] Chen, X., Zhou, X., Cheng, R., Song, C., Zhang, J., Wu, Y., Ba, Y., Li, H., Sun, Y., You, Y., Zhao, Y., and Pan, F., Electric field control of Néel spin-orbit torque in an antiferromagnet. *Nat. Mater.* **18**, 931 (2019).
- [19] Grigorev, V., Filianina, M., Lytvynenko, Y., Sobolev, S., Pokharel, A. R., Lanz, A. P., Sapozhnik, A., Kleibert, A., Bodnar, S., Grigorev, P., Skourski, Y., Kläui, M., Elmers, H.-J., Jourdan, M. and Demsar, J., Optically Triggered Néel Vector Manipulation of a Metallic Antiferromagnet Mn₂Au under Strain. *ACS Nano* **XXXX**, XXX, (2022). <https://doi.org/10.1021/acsnano.2c07453>
- [20] Bodnar, S. Yu., Filianina, M., Bommanaboyena, S. P., Forrest, T., Maccherozzi, F., Sapozhnik, A. A., Skourski, Y., Kläui, M., and Jourdan, M. Imaging of current induced Néel vector switching in antiferromagnetic Mn₂Au. *Phys. Rev. B* **99**, 140409(R) (2019).
- [21] Wadley, P., Reimers, S., Grzybowski, M. J., Andrews, C., Wang, M., Chauhan, J. S., Gallagher, B. L., Campion, R. P., Edmonds, K. W., Dhesi, S. S., Maccherozzi, F., Novák, V., Wunderlich, J., and Jungwirth, T. Current polarity-dependent manipulation of antiferromagnetic domains *Nat. Nanotech.* **13**, 632 (2018).
- [22] Meer, H., Schreiber, F., Schmitt, C., Ramos, R., Saitoh, E., Gomonay, O., Sinova, J., Baldrati, L., and Kläui, M. Direct Imaging of Current-Induced Antiferromagnetic Switching Revealing a Pure Thermomagnetoelastic Switching Mechanism in NiO. *Nano Lett.* **21**, 114 (2021).
- [23] Barthem, V. M. T. S., Colin, C. V., Mayaffre, H., Julien, M.-H., and Givord, D. Revealing the properties of Mn₂Au for antiferromagnetic spintronics. *Nat. Commun.* **4**, 2892 (2013).
- [24] Salemi, L., Berritta, M., Nandy, A., K., Oppeneer, P. M. Orbitaly dominated Rashba-Edelstein effect in noncentrosymmetric antiferromagnets. *Nat. Commun.* **10**, 5201 (2019).
- [25] Selzer, S., Salemi, L., Deák, A., Szunyogh, L., Oppeneer, P., M., and Nowak, U., Current-induced switching of antiferromagnetic order in Mn₂Au from first principles. *Phys. Rev. B* **105**, 174416 (2022).
- [26] Reimers, S. et al., manuscript in preparation (2022).

- [27] Bodnar, S. Yu., Skourski, Y, Gomonay, O., Sinova, J., Kläui, M., and Jourdan, M., Magnetoresistance Effects in the Metallic Antiferromagnet Mn_2Au . *Phys. Rev. Appl.* **14**, 014004 (2020).
- [28] Bommanaboyena, S. P., Bergfeldt, T., Heller, R., Kläui, M., and Jourdan, M. High quality epitaxial Mn_2Au (001) thin films grown by Molecular Beam Epitaxy. *J. Appl. Phys.* **127**, 243901 (2020).
- [29] Bommanaboyena, S. P., Backes, D., Veiga, L. S. I., Dhesi, S. S., Niu, Y. R., Sarpi, B., Denneulin, T., Kovács, A., Mashoff, T., Gomonay, O., Sinova, J., Everschor-Sitte, K., Schönke, D., Reeve, R. M., Kläui, M., Elmers, H.-J., and Jourdan, M., Readout of an antiferromagnetic spintronics system by strong exchange coupling of Mn_2Au and Permalloy. *Nat. Commun.* **12**, 2829 (2021).